

Synthesizing Lattice Structure in Phase Space

Lingzhen Guo^{1,2} and Michael Marthaler^{1,2}

¹*Institut für Theoretische Festkörperphysik, Karlsruhe Institute of Technology, 76128 Karlsruhe, Germany*

²*DFG-Center for Functional Nanostructures (CFN), Karlsruhe Institute of Technology, 76128 Karlsruhe, Germany*

(Dated: October 2, 2018)

We consider a realistic model, i.e., ultracold atoms in a driven optical lattice, to realize phase space crystals¹. The corresponding lattice structure in phase space is more complex and contains rich physics. A phase space lattice differs fundamentally from a lattice in real space, because its coordinate system, i.e., phase space, has a noncommutative geometry, which naturally provides an artificial gauge (magnetic) field. We study the behavior of the quasienergy band structure as function of the artificial magnetic field and investigate the thermal properties. Synthesizing lattice structures in phase space is not only a new way to create artificial lattice in experiments but also provides a platform to study the intriguing phenomena of driven systems far away from equilibrium.

PACS numbers: 67.85.-d, 42.65.Pc, 03.65.-w, 05.45.-a

I. INTRODUCTION

In a recent paper¹, we introduced the idea of phase space crystals, i.e., a lattice structure in phase space created by breaking a continuous phase rotational symmetry via a driving field. In our previous work we used the model of ultracold atoms trapped in a time-dependent power-law potential, i.e., $\sim x^n \cos(\omega_d t)$, to illustrate our idea. However, this model is technically difficult to realize in experiments. Here, we present a realistic driven optical lattice model, i.e., the power-law driving is replaced by a cosine-type driving, i.e., $\sim \cos(kx + \omega_d t)$, to realize phase space crystals. Thus, the novel phenomena predicted by phase space crystals can be directly observed in current experiments of ultracold atoms in an optical lattice.

The model proposed here synthesizes a more complex lattice structure in phase space and thus contains rich physics. We further develop the theory of phase space crystals and calculate the complex quantum tunnelling rates. We identify the artificial (magnetic) gauge field in phase space, which is a result of the noncommutative geometry of the phase space crystal. Compared to the artificial lattice structures in real space²⁻⁹, synthesizing a lattice structure in phase space has the key advantage of being conveniently tunable in experiments through changes in the driving field. Due to this possibility phase space lattices may provide a new platform to simulate condensed matter phenomena.

II. MODEL AND HAMILTONIAN

The model we propose here can be realized by ultracold atoms trapped in a time-dependent optical lattice. The Hamiltonian is given by

$$H(t) = \frac{p^2}{2m} + \frac{1}{2}m\omega^2 x^2 + 2A \cos(kx + \omega_d t). \quad (1)$$

Here, the parabolic term is the harmonic confinement potential of ultracold atoms, which can be created by a gaussian beam profile of a laser¹⁰ or introduced by another external field. As sketched in Fig. 1, the characteristic length of the

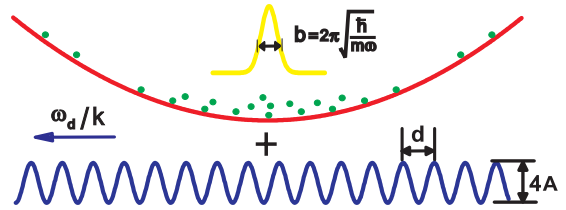


FIG. 1: **Ultracold atoms in driven optical lattice.** Ultracold atoms (green dots) are confined in a harmonic potential (red parabolic curve). The ground state of confinement potential is represented by a Gaussian wave packet (yellow wave packet) with width $b = \sqrt{\hbar/(m\omega)}$. The blue curve represents a propagating optical lattice with period d , amplitude $2A$ and velocity ω_d/k . The potential for creating phase space lattice is the sum of them.

ground state in the confinement potential is $b = 2\pi \sqrt{\hbar/(m\omega)}$. Experimentally the optical lattice is created by the interference of two counter-propagating laser beams, which form an optical standing wave with period $d = 2\pi/k$. The ultracold atoms are trapped by the interaction between the laser light field and the oscillating dipole moment of atoms induced by the laser light¹¹. We can drive the optical lattice simply by tuning the phase difference of the two laser beams linearly as described by Hamiltonian (11). Effectively, this creates a propagating optical lattice with a velocity of ω_d/k . An important parameter is $\lambda \equiv (b/d)^2 = \hbar k^2/(m\omega)$, which defines the “quantumness” of our system. It is large in the quantum regime and goes to zero in the semiclassical limit. We emphasize that the optical potential is time-dependent and the confinement potential also plays an important role. Thus, our system does not have spatial periodicity and the Bloch theory in real space does not apply directly for the Hamiltonian (11).

We are interested in the regime near the high-order resonant condition $\omega_d \approx n\omega$ with a large integer $n \gg 1$. For the duration of this paper we will use $n = 30$. The detuning $\delta\omega \equiv \omega - \omega_d/n$ is much smaller than the natural frequency ω . We perform a unitary transformation of the Hamiltonian $H(t)$ via the operator $\hat{U} = e^{i(\omega_d/n)\hat{a}^\dagger \hat{a} t}$, where \hat{a} is the annihilation operator of the oscillator. In the spirit of the rotating wave approximation (RWA), we drop the fast oscillating terms and

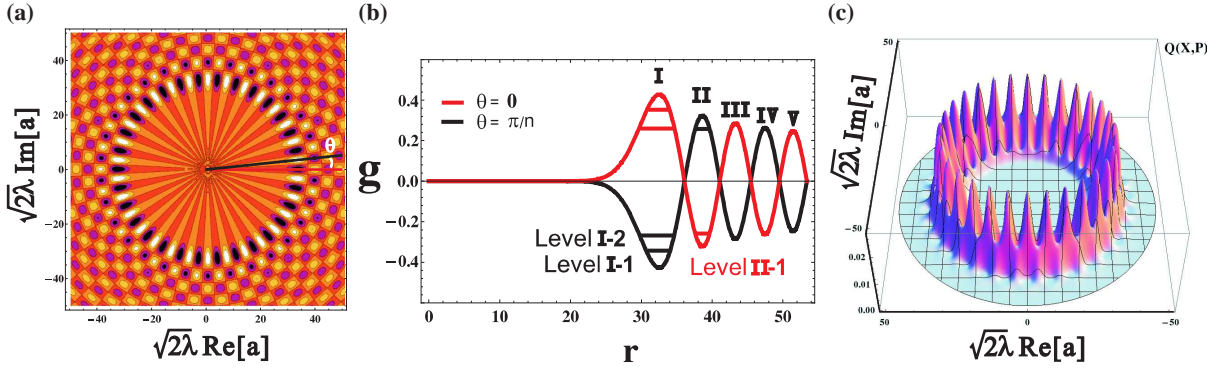


FIG. 2: **Phase space lattice with $n=30$:** a) Lattice structure with n -fold symmetry in phase space by plotting Hamiltonian (2) in the semiclassical limit. The color represents the value of quasienergy g , which indicates the whole lattice is composed of two identical sublattices because of the chiral symmetry for $\delta\omega = 0$. b) Quasienergy along the radius direction with angle $\theta = 0$ and $\theta = \pi/n$. The roots of $g(r) = 0$ divide the whole lattice into many loops, which are labelled by Roman numerals as indicated on the top of this figure. The corresponding localized quantum states inside the loops are labelled by *Level I-1*, *Level I-2*, *Level II-1*, etc. c) Q -function of a quasiumber state with quasiumber $m = 0$. The periodicity of Q -function reflects the n -fold symmetry of phase space lattice.

arrive at the time-independent Hamiltonian (see more details in section A of the Appendix)

$$\hat{g} = \lambda\epsilon(\hat{a}^\dagger\hat{a} + \frac{1}{2}) + \mu\left[\left(\frac{\lambda}{2}\right)^{-\frac{n}{2}} e^{-\frac{\lambda}{2}\hat{a}^\dagger} \hat{a}^n L_{\hat{a}^\dagger\hat{a}}^{(-n)}\left(\frac{\lambda}{2}\right) + h.c.\right]. \quad (2)$$

In the context of Floquet theory, \hat{g} is called *quasienergy*^{14,20}, which has been scaled by the energy $m(\omega/k)^2 = \hbar\omega/\lambda$. The parameters $\epsilon \equiv \delta\omega/\omega$ and $\mu \equiv \lambda A/(\hbar\omega)$ are the dimensionless detuning and driving strength respectively. Functions $L_{\hat{a}^\dagger\hat{a}}^{(-n)}(\bullet)$ are the generalized Laguerre polynomials, as a function of the photon number $\hat{a}^\dagger\hat{a}|k\rangle = k|k\rangle$, where $|k\rangle$ are the Fock states.

III. SYMMETRIES

In the following, we are particularly interested in the resonant condition, i.e., the detuning is zero $\delta\omega = 0$. Without loss of generality, we set the scaled driving strength to unity, i.e., $\mu = 1$. In this case, the RWA Hamiltonian (2) has two new symmetries which are not visible in the original Hamiltonian (11). To visualize them, we replace the operator \hat{a} by a complex number in the semiclassical limit and plot the quasienergy g in the phase space spanned by $\text{Re}[a]$ and $\text{Im}[a]$. As displayed in Fig. 2(a), we first see the *discrete angular symmetry* $g(\theta) = g(\theta + 2\pi/n)$. Additionally we have the *chiral symmetry* $g(\theta) = -g(\theta + \pi/n)$, which divides the whole lattice structure into two identical sublattices as indicated in Fig. 2(a) by the different colors. To describe the two symmetries in quantum mechanics, we define a unitary operator $\hat{T}_\tau = e^{-i\tau\hat{a}^\dagger\hat{a}}$ with the properties $\hat{T}_\tau^\dagger\hat{a}\hat{T}_\tau = \hat{a}e^{-i\tau}$ and $\hat{T}_\tau^\dagger\hat{a}^n\hat{T}_\tau = \hat{a}^ne^{-in\tau}$. Since the operator $\hat{a}^\dagger\hat{a}$ keeps invariant under the transformation of \hat{T}_τ , it is not difficult to check that the RWA Hamiltonian (2) is invariant under discrete transformation $T_\tau^\dagger\hat{g}T_\tau = \hat{g}$ for $\tau = 2\pi/n$. We call this symmetry *discrete phase translation symmetry*. The chiral symmetry follows from the fact $T_\tau^\dagger\hat{g}T_\tau = -\hat{g}$ for $\tau = \pi/n$. The chiral symmetry suggests that the two sublattices are symmetric

with respect to $g = 0$, except a phase shift $\theta \rightarrow \theta + \pi/n$. The angular symmetry indicates it is convenient to introduce the radial and angular operators \hat{r} and $\hat{\theta}$ via $\hat{a} = e^{-i\hat{\theta}}\hat{r}/\sqrt{2\lambda}$ and $\hat{a}^\dagger = \hat{r}e^{i\hat{\theta}}/\sqrt{2\lambda}$. They obey the commutation relation

$$[\hat{r}^2, e^{i\hat{\theta}}] = 2\lambda e^{i\hat{\theta}} \quad (3)$$

where λ plays the role of a dimensionless Plank constant.

IV. PHASE SPACE LATTICE

In the semiclassical limit $\lambda \rightarrow 0$, the quantum Hamiltonian \hat{g} can be written in its classical form (see more details in section A of the Appendix)

$$g = \frac{1}{2}\epsilon r^2 + 2\mu J_n(r) \cos(n\theta - \frac{n\pi}{2}). \quad (4)$$

Here, we have used the asymptotic property of Laguerre polynomials, i.e., $\lim_{k \rightarrow \infty} L_k^{(n)}(x/k) = k^n e^{\frac{x}{k}} x^{-n/2} J_n(2\sqrt{x})$, where $J_n(\bullet)$ is the Bessel function of order n . The angular periodicity comes from the cosine function in Eq.(4) while the radial structure is created by the Bessel function $J_n(r)$. A similar situation has recently been studied in voltage biased Josephson junctions^{12,13}. The zero lines of g form the “cells” of the phase space lattice as shown in Fig. 2(a). The center of each cell is a stable point corresponding to either a local minimum or a local maximum of g (see more details in section C of the Appendix). The area inside the cell represents the basin of attraction for the stable state in the center. In Fig. 2(b), we show the radial structure of the quasienergy g by plotting it along two angular directions $\theta = 0$ and $\theta = \pi/n$. We see the quasienergy oscillates as a function of the radius r in the form of Bessel functions $J_n(r)$. We divide the whole lattice structure into “loops”, which correspond to ring-like areas in Fig. 2(a) between two radii which satisfy $J_n(r) = 0$. We label them from inside to outside by Roman numerals *I*, *II*, *III* and so on as indicated in Fig. 2(b).

V. QUASINUMBER THEORY

We diagonalize the quantum Hamiltonian (2) and study the properties of its quasienergy spectrum. With zero detuning $\delta\omega = 0$, and driving $\mu = 1$, the spectrum is only determined by the effective Planck constant λ . In Fig. 3(a) we show the structure of the quasienergy spectrum as function of the parameter $1/\lambda$. It is clear that the quasienergy spectrum is symmetric with respect to $g = 0$ because of the chiral symmetry. We also see that gaps in the spectrum are opened for small λ and disappear for sufficiently large λ . The transition happens around $\lambda \approx 5$. We will calculate the gaps using WKB theory and discuss the physical mechanism of gap closing below.

In Fig. 3(b) we show the gapless quasienergy spectrum for $\lambda = 6$ and the band structure of the spectrum for $\lambda = 4$. The band structure comes from the discrete phase translation symmetry. We introduce the quasinumber theory¹ according to Bloch's theorem. Due to $\hat{T}_\tau^\dagger \hat{g} \hat{T}_\tau = \hat{g}$ for $\tau = 2\pi/n$, the eigenstates $\psi_m(\theta)$ of the quasienergy Hamiltonian, $\hat{g}\psi_m(\theta) = g(m)\psi_m(\theta)$, have the form $\psi_m(\theta) = \varphi_m(\theta)e^{-im\theta}$, with a periodic function $\varphi_m(\theta + \tau) = \varphi_m(\theta)$. Here, the integer number m is called *quasi-number*, which is conjugate to the phase θ . It is an analogue of the quasi-momentum \vec{k} in a crystal. In Fig. 3(c), we plot the quasienergy band structure in the reduced Brillouin zone $m\tau \in [0, 2\pi)$. We count the bands from the bottom and relabel the eigenstates $\psi_m(\theta)$ by $\psi_{l,m}(\theta)$, where the subscript $l = 1, 2, \dots$ indicates the band that the eigenstate belongs to.

In Fig. 3(d), we plot the occupation number statistics of Fock states, i.e., $P_{l,m}(k) = |\langle k | \psi_{l,m}(\theta) \rangle|^2$, for quasinumber states with $m = 0$ and $m = 15$ in the first band $l = 1$. As we can see from the probability distribution, the quasinumber states are the superposition of Fock states with photon numbers being multiples of n . To visualize the quasinumber states, we plot the Q -function of state $\psi_{1,0}(\theta)$ in Fig. 2(c). The Q -function is a quasi-probability distribution in phase space¹⁵ defined by $Q(\alpha, \alpha^*) \equiv |\langle \alpha | \psi_{l,m}(\theta) \rangle|^2 / \pi$, where $|\alpha\rangle$ is the coherent state given by $\hat{a}|\alpha\rangle = \alpha|\alpha\rangle$ or $|\alpha\rangle = e^{-|\alpha|^2/2} \sum_{k=0}^{\infty} \alpha^k / \sqrt{k!} |k\rangle$. The crystalline structure of Q -function in angular direction reflects the n -fold discrete phase translation symmetry.

From the form of the Q -function we see that the eigenstates of the system $\psi_m(\theta)$ are delocalized states in phase space, which are superposition of localized states corresponding to the discrete energy levels as indicated in Fig. 2(b). We label these levels in the first loop by *Level I - 1*, *Level I - 2* and those in the second loop *Level II - 1* etc. In the semiclassical limit, these quantum levels become classical orbits of iso-quasienergy contours represented by the boundaries of the colored elliptical areas inside each cell as shown in Fig. 2(a). The shapes of these orbits vary in different loops as displayed on the top of Fig. 4(d).

VI. QUASIENERGY BAND STRUCTURE

The formation of quasienergy bands near the bottom can be understood in the frame of the tight-binding model. If we ne-

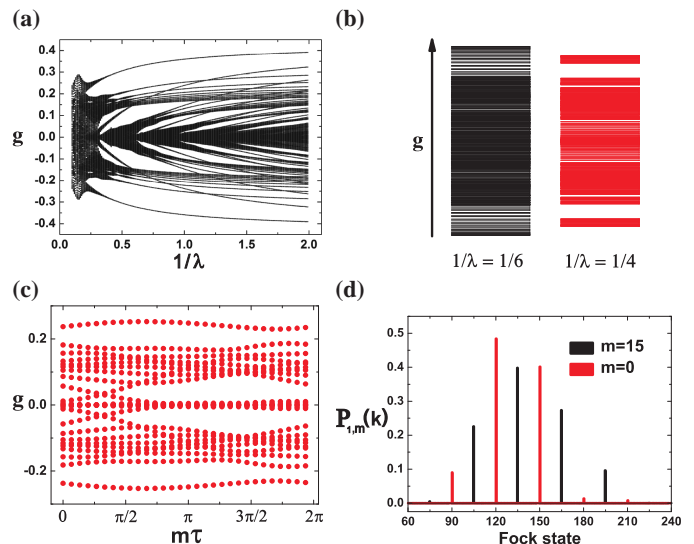


FIG. 3: **Quasienergy band structure:** a) Quasienergy spectrum of Hamiltonian (2) as function of parameter $1/\lambda$. The gap closes at $\lambda \approx 5$. b) Gapless quasienergy spectrum with parameter $\lambda = 6$ and gapped spectrum $\lambda = 4$. Parameter m is the quasinumber of each state. c) The quasienergy band structure in the reduced Brillouin zone with $\lambda = 4$. The parameter $\tau = 2\pi/n$ is the angular lattice constant. d) Probability distribution over Fock states of quasinumber states in the bottom band with $m = 0$ (red) and $m = 15$ (black) respectively.

glect quantum tunnelling, the n localized states in each loop are n degenerate states. If we consider quantum tunnelling, they are broadened and form bands. We can label the bands by the labels of corresponding localized levels, e.g., the bottom band of the whole quasienergy spectrum is *Band I - 1*. We can describe the structure of the l -th tight-binding band approximately by

$$g_l(m) = E_l - 2|J_l| \cos(m\tau + \delta_l\tau). \quad (5)$$

Here, E_l represents the center of the l -th band and the quasienergy of the corresponding localized level. The l -th bandwidth d_l is determined by the tunnelling rate, i.e., $d_l = 4|J_l|$. From Fig. 3(c) we see that the bands are not symmetric with respect to the center of the Brillouin zone in general. We describe the asymmetry by an *asymmetry factor* δ_l . The asymmetry factor comes from the fact that the two dimensions of phase space are not commutative. We will calculate the gaps, bandwidths and asymmetry factor by WKB theory below.

A. Quantum tunnelling in phase space

From the commutation relation (3), it can be shown that $[\hat{p}^2/2, \hat{\theta}] \approx i\lambda$ in the region of $r \gg 1$. We can view operators $\hat{p}^2/2$ and $\hat{\theta}$ as “coordinate” and “momentum” respectively, i.e., $\hat{\theta} \approx -i\lambda r^{-1} \partial/\partial r$. In the semiclassical limit, the variables $r^2/2$ and θ define the phase space for our WKB calculation. In Fig. 4(a), we plot the quasienergy g in the range of $\theta \in [-2\pi/n, 2\pi/n]$. For a fixed g , all the branches of classical

orbits are given by

$$\theta_{\pm}(r, g) = \frac{\pi}{2} \pm \frac{1}{n} \arccos \left[\frac{g - \epsilon r^2/2}{2\mu J_n(r)} \right] + k \frac{2\pi}{n}, \quad (6)$$

where k takes integers $0, 1, 2, \dots$, and $n - 1$. Two real solutions $\theta_{\pm}(\xi, g)$ together represent one closed classical orbit. There are n identical orbital branches with only a $2\pi/n$ -shift of θ . From the condition $|(g - \epsilon r^2/2)/[2\mu J_n(r)]| < 1$, we can determine the boundaries of classical motion. In Fig. 4(a), we indicate the boundaries of classical motion by $r_1^2/2, r_2^2/2$ and $r_3^2/2$ in the phase space spanned by $r^2/2$ and θ . The region between $r_2^2/2$ and $r_3^2/2$ is the classically forbidden region for the fixed quasienergy g . In the quantum regime, however, the states can tunnel into each other. In Fig. 4(a), we show how the two neighboring *Level I* - 1 states tunnel into each other through phase space. The main tunnelling path with least action is indicated by the white arrows in the same plot. The optimal path is to tunnel first into the nearest region in *Loop II* across one saddle point (white dot) and then tunnel back to the neighboring *Level I*-1 across another saddle point. There also exist many other possible tunnelling paths in phase space, e.g., the path indicated by yellow arrows in Fig. 4(a). But the contributions from these paths are exponentially small compared to the main tunnelling path (see more details in section B of the Appendix).

B. Quasienergy levels and bandwidths

From the WKB theory, we know the phase space area enclosed by the classical orbit is quantized according to the so called Bohr-Sommerfeld quantization condition¹⁶

$$\begin{aligned} S(g) &= \frac{2}{n} \int_{r_1}^{r_2} \arccos \left[\frac{g - \epsilon r^2/2}{2\mu J_n(r)} \right] r dr \\ &= 2\pi\lambda(k + \frac{1}{2}), \end{aligned} \quad (7)$$

where k takes nonnegative integers. From the above condition we can calculate the quasienergy levels. As shown in Fig.4(b), the left subfigure shows several lowest levels calculated using the quantization condition (7). We compare our WKB calculation to the numerical simulation. The agreement is very good. Noticeably, *Level I*-2 and *Level II*-1 cross each other near $\lambda = 1.2$. The level crossing has significant effect on the bandwidths as we discuss below.

The width of the l -th band d_l is given by the tunnelling rate J_l , i.e., $d_l = 4|J_l|$. The amplitude of J_l is given by the integral of the imaginary part of ‘‘momentum’’ θ in the classical forbidden region $r_2 < r < r_3$

$$|J_l| = \frac{\lambda}{2\pi} \left(\frac{dS}{dg} \right)^{-1} \Big|_{g=g_l} \exp \left(- \frac{2}{\lambda} \int_{r_2}^{r_3} \text{Im}[\theta] r dr \right). \quad (8)$$

Here, $S(g)$ in the prefactor as function of g is given by the first equality of Eq.(7). In section B of the Appendix, we give a detailed description of the behavior of $\text{Im}[\theta]$ in the classical forbidden region. Here we just present our results. In

Fig. 4(b) we show the bandwidths of *Level I*-1 and *Level I*-2 calculated by Eq.(34) and compare them to the numerical calculation. There is a cusp in the curve of *Level I*-2. This happens because of the crossing of *Level I*-2 and *Level II*-1 which significantly enhances the quantum tunnelling of *Level I*-2. In this case, we need to consider three interacting levels, i.e., two neighboring *Level I*-2 states and the medium state of *Level II*-1 as indicated by the closed orbits in Fig. 4(a). The Hamiltonian of three interacting levels (TIL) is described by the following 3×3 matrix

$$H_{TIL} = \begin{pmatrix} g_1 & J_{12} & J_{11} \\ J_{12} & g_2 & J_{12} \\ J_{11} & J_{12} & g_1 \end{pmatrix}.$$

Here g_1, g_2 represent the quasienergies of *Level I*-2 and *Level II*-1 respectively. Parameter J_{11} represents the tunnelling rate between the two neighboring *Level I*-2 states. Parameter J_{12} represents the tunnelling rate between the state of *Level I*-2 and the state of *Level II*-1. The tunnelling rate J_{11} is given by Eq.(34) by taking $g = g_1$, while the tunnelling rate J_{12} is given by

$$J_{12} = \frac{\lambda}{2\pi} \left(\frac{dS}{dg} \right)^{-1} \Big|_{g=g_2} \exp \left(- \frac{1}{\lambda} \int_{r_2}^{r_3} \text{Im}[\theta] r dr \right). \quad (9)$$

We can get the modified quasienergy levels by diagonalizing the matrix H_{TIL} . The level spacing Δ_{11} of the two modified *Level I*-2 states gives the effective tunnelling rate between them. Therefore, the correct bandwidth of *Band I*-2 is $2\Delta_{11}$.

C. Band asymmetry and artificial magnetic field

From Fig. 3(c), we see that the quasienergy bands are not symmetric with respect to the center of the reduced Brillouin zone. The asymmetry is described by the asymmetry factor δ_l . In the frame of tight-binding approximation, the Bloch eigenstate $\psi_{lm}(\theta)$ is given by $\psi_{lm}(\theta) = 1/\sqrt{n} \sum_{q=0}^{n-1} e^{imq\tau} \hat{T}_{\tau}^q \phi_l(\theta)$, where $\phi_l(\theta)$ is the localized wave functions forming the band. The quantum tunnelling rate can be calculated by $J_l = - \int [\hat{T}_{\tau} \phi_l(\theta)]^* \hat{g} \phi_l(\theta)$. The corresponding quasienergy spectrum of the l -th band then is $g_l(m) = \int_0^{2\pi} \psi_{lm}^*(\theta) \hat{g} \psi_{lm}(\theta) d\theta \approx E_l - J_l e^{im\tau} - J_l^* e^{-im\tau}$. The band asymmetry comes from the fact that quantum tunnelling rate J_l in driven systems is generally a complex number^{1,17}, i.e., $J_l = |J_l| e^{-i\delta_l\tau}$, and the phase parameter δ_l is exactly the asymmetry factor. We can calculate the phase δ_l using the WKB theory we developed above.

In fact, when r is approaching one of the roots $r^{(0)}$ with $J_n(r^{(0)}) = 0$, from Eq.(31) we see the amplitude of ‘‘momentum’’ θ goes to infinity $|\theta(r^{(0)})| \rightarrow \infty$. This means the WKB approximation breaks down near the root of the Bessel function $J_n(r^{(0)}) = 0$ and we need a connecting condition. Because $r^{(0)} \gg 1$, we can expand the phase translation operator $\hat{T}_{\tau} = e^{-i\hat{a}\tau} \hat{a}^{\dagger} \hat{a}$ by $\hat{a}^{\dagger} \hat{a} \approx \lambda^{-1}(r^{(0)})^2/2 + i\partial/\partial\theta$ and the connecting condition, i.e., the neighboring localized state of $\phi_l(\theta)$, is given by $\hat{T}_{\tau} \phi_l(\theta) \approx e^{-i\lambda^{-1}(r^{(0)})^2\tau/2} \phi_l(\theta + \tau)$. Thus we get the symmetry factor $\delta_l = \delta_l^0 + \lambda^{-1}(r^{(0)})^2/2$, where δ_l^0 is the residual asymmetry beyond WKB calculation and can be removed

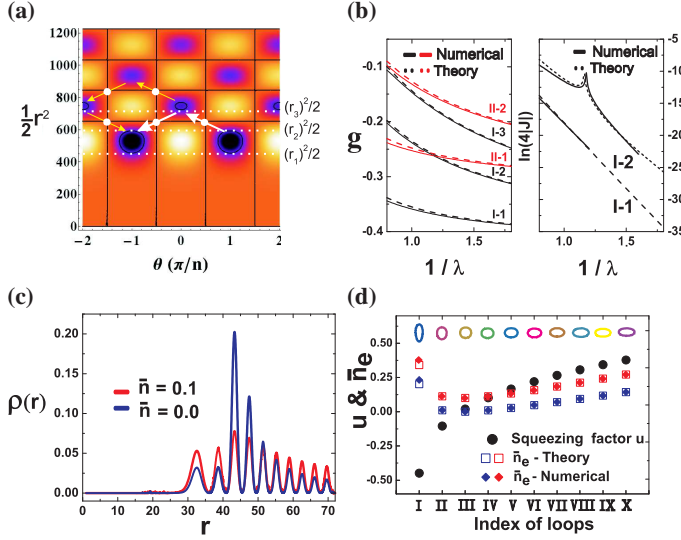


FIG. 4: **Quantum tunnelling and Thermal distribution:** a) Quantum tunnelling processes in phase space spanned by variables $r^2/2$ and θ . We plot the quasienergy g in the interval $\theta \in [-\pi/n, \pi/n]$. White dots are the unstable saddle points. White arrows indicate the main tunnelling path of two neighbored Level I-1 states and the yellow arrows indicate other possible tunnelling paths. b) The quasienergy levels (left) and bandwidths (right) from WKB calculation (dashed lines) and numerical simulations (solid lines). c) Density function of stationary distribution along the radius r at different temperatures. d) The squeezing factor u and effective temperature \bar{n}_e of the first ten loops of phase space lattice. The colored circles on the top represent the shapes of classical orbits near the bottom of each loop, which reflect the squeezing factor u .

by redefining the phase translation operator $\hat{T}_\tau = e^{-i\tau(\hat{a}^\dagger \hat{a} - \delta_l^0)}$. The asymmetry factor δ_l is linearly dependent on the parameter $1/\lambda$ with the slope $(r^{(0)})^2/2$ differing between bands. If we count $r^{(0)} = 0$ as the first root of $J_n(r)$, then the asymmetry factors of bands in the l -th ($l \geq 2$) loop are all given by the l -th ($l \geq 2$) root of the Bessel function. But the asymmetry factors of the bands in the first loop are determined by the second root of the Bessel function. The reason is that the localized states inside the first loop tunnel through its upper boundary while states in other loops tunnel through lower boundaries. In section B of the Appendix, we give more detailed discussion on tunnelling paths and show more results about the linear relationship between δ_l versus $1/\lambda$ for different bands.

The fact that the tunnelling amplitudes are complex means there is an artificial magnetic field B_{eff} in phase space. Imagine we have a loop of atoms forming a one dimensional lattice in real space with magnetic field B across the loop. The magnetic field induces an additional phase to the tunnelling amplitude between neighbored atoms $J = |J|e^{-i\delta}$, where $\delta \propto B$ is called Peierls phase¹⁸. Comparing the Peierls phase to the asymmetry factor of the phase space lattice calculated above, we can identify there is an effective magnetic field $B_{eff} \propto 1/\lambda$ in phase space. The coordinate system of a phase space lattice has a noncommutative geometry¹⁹, which is fundamentally different from spatial lattices. It is this noncommutative phase space which creates an artificial magnetic field and is responsible for the asymmetry of the quasienergy band structure.

VII. DISSIPATIVE DYNAMICS

The above calculation of the quasienergy bandstructure does not consider the dissipative environment. In actual experiments, due to the quantum and thermal fluctuations, the dynamics in a phase space lattice is non-unitary. For a driven system, we can measure the non-equilibrium stationary state in experiments. We use the master equation method to describe the dissipative evolution caused by thermal and quantum fluctuations. Already previously it has been shown that a Lindblad type of master equation²⁰⁻²³ is sufficient as description,

$$\frac{\partial \rho}{\partial t} = -\frac{i}{\lambda} [\hat{g}, \rho] + \kappa(1 + \bar{n})\mathcal{D}[a]\rho + \kappa\bar{n}\mathcal{D}[a^\dagger]\rho, \quad (10)$$

where the time t is dimensionless and scaled by the natural frequency ω . The Lindblad superoperator is defined through $\mathcal{D}[A]\rho \equiv A\rho A^\dagger - (A^\dagger A\rho + \rho A^\dagger A)/2$, $\bar{n} = (e^{\hbar\omega_0/k_B T} - 1)^{-1}$ is the Bose distribution and κ is the dimensionless damping also scaled ω .

Based on the master equation (43), we calculate the density matrix of the stationary distribution in the basis of the Fock states $\{|k\rangle, k = 0, 1, \dots\}$. By the relationship of $k = r^2/(2\lambda)$, we can find the probability density along a circle with radius r , i.e., $\rho(r) = r\lambda^{-1}\langle k|\rho|k\rangle$. In Fig 4(c), we plot $\rho(r)$ for different temperatures $\bar{n} = 0$ and $\bar{n} = 0.1$. We see that $\rho(r)$ oscillates with radius r . The zero nodes of $\rho(r)$ actually correspond to the boundaries of phase space lattice loops. Because the quantum heating²⁴ of each loop is not the same, the probabilities over the loops are not equally distributed. On the bottom of each loop, the stationary distribution can be described by an effective temperature \bar{n}_e . The localized ground state of each loop can be approximately described by a squeezed state with the squeezing factor u and the corresponding effective temperature is given by $\bar{n}_e = |u|^2 + \bar{n}(2|u|^2 + 1)$ (see more details in section D of the Appendix). In our case, as we can see from Fig 4(c), the peak of $\rho(r)$ is in the third loop. The reason is the effective temperature of the third loop is lower than other loops. In Fig 4(d), we calculate the squeezing factor u and the effective temperature \bar{n}_e for the first ten loops and compare them to fully numerical simulations. The agreement is very good. Another interesting fact is the squeezing factor u changes from a negative value to a positive value. This means the shape of the squeezed state in each loop is different as displayed by the colored orbits on the top of Fig 4(d). The orbital shapes are taken from the plot in Fig. 2(a). The third orbit is very close to a round circle, which means the squeezing factor $u \approx 0$ and the resulting effective temperature $\bar{n}_e \approx \bar{n}$. The stationary distribution can be directly measured in the experiments²⁵.

VIII. DISCUSSION

The phase space lattice can also realized in circuit-QED systems, i.e., a superconducting cavity coupled to Josephson junctions. The Hamiltonian is $H_{cQED} = \hbar\omega a^\dagger a + 2E_J \cos(4\pi e\hbar^{-1}\Phi) \cos\varphi$. The Josephson junction can be

driven by either a dc voltage^{12,13}, which creates $\varphi = \varphi_0 + \omega_d t$ with $\omega_d = 2eV/\hbar$, or a time-dependent magnetic flux²⁶ $\Phi = \omega_d t/(4\pi e\hbar^{-1})$. The effective Planck constant in this case is $\lambda = 8\pi\omega L/(h/e^2)$, where L is the inductance of the circuit and $h/e^2 \approx 25.8 \text{ k}\Omega$ is the von Klitzing constant. The typical impedance ωL of circuit-QED systems using only geometrical inductors and capacitors, can not exceed the characteristic impedance of vacuum $\mu_0 c \approx 376.73 \text{ }\Omega$ ²⁷, which means that we have $\lambda < 0.015$ in circuit-QED systems. However, there are several proposals to realized a super-inductance based on the design of Josephson junction arrays^{27,28} which can increase the impedance significantly up to $35 \text{ k}\Omega$ resulting $\lambda > 1$. Thus, it is possible to realize phase space lattices in circuit-QED systems combined with a proper design of Josephson junction arrays.

Acknowledgements

We acknowledge helpful discussions with Dr. P. Kotetes, Dr. P. Jin, Prof. G. Johansson, Prof. G. Schön, Prof. F. Marquart and Dr. V. Peano.

Supplemental Material

A. Hamiltonians

In this section, we give detailed derivation from the time-dependent Hamiltonian (1) to the RWA Hamiltonian (2) and the semiclassical Hamiltonian (4) in the main text. To be convenient, we write the original Hamiltonian of ultracold in the driven optical lattice atoms here again

$$H_{DOL} = \frac{p^2}{2m} + \frac{1}{2}m\omega^2 x^2 + 2A \cos(kx + \omega_d t). \quad (11)$$

Now, we introduce a , a^\dagger via $x = \sqrt{\hbar/(2m\omega)}(a^\dagger + a)$ and $p = i\sqrt{m\hbar\omega/2}(a^\dagger - a)$. By introducing parameter $\lambda \equiv \hbar k^2/(m\omega)$, we map the Hamiltonian (11) to the following

$$H(t) = \hbar\omega a^\dagger a + 2A \cos\left[\sqrt{\frac{\lambda}{2}}(a^\dagger + a) + \omega_d t\right]. \quad (12)$$

We introduce the scaled coordinate and momentum operators $\hat{Q} = \sqrt{\frac{\lambda}{2}}(a^\dagger + a)$ and $\hat{P} = i\sqrt{\frac{\lambda}{2}}(a^\dagger - a)$ with the noncommutative relationship $[\hat{Q}, \hat{P}] = i\lambda$. We write Hamiltonian (12) in an alternative form

$$H(t) = \frac{1}{2\lambda}\hbar\omega(\hat{Q}^2 + \hat{P}^2) + 2A \cos(\hat{Q} + \omega_d t), \quad (13)$$

Now, we employ an unitary operator $U = e^{i\hbar\frac{\omega_d}{\pi}a^\dagger a t}$ to transform Hamiltonian (13) into a rotating frame with frequency

ω_d/n

$$\begin{aligned} H_{RF} &= UH(t)U^\dagger - iUU^\dagger \\ &= \frac{1}{2\lambda}\hbar\delta\omega(\hat{Q}^2 + \hat{P}^2) + 2AU \cos(\hat{Q} + \omega_d t)U^\dagger \\ &= \frac{1}{2\lambda}\hbar\delta\omega(\hat{Q}^2 + \hat{P}^2) + (Ae^{i\omega_d t}Ue^{i\hat{Q}}U^\dagger + h.c.) \\ &= \frac{1}{2\lambda}\hbar\delta\omega(\hat{Q}^2 + \hat{P}^2) + \{Ae^{i\omega_d t}e^{i[\hat{Q}\cos(\omega_d t/n) + \hat{P}\sin(\omega_d t/n)]} + h.c.\} \\ &\equiv \frac{1}{2\lambda}\hbar\delta\omega(\hat{Q}^2 + \hat{P}^2) + [Ae^{i\omega_d t}M(\hat{Q}, \hat{P}) + h.c.]. \end{aligned} \quad (14)$$

Here, we define $M(\hat{Q}, \hat{P}) \equiv e^{i[\hat{Q}\cos(\omega_d t/n) + \hat{P}\sin(\omega_d t/n)]}$ and the detuning $\delta\omega \equiv \omega_0 - \omega_d/n$. To calculate the matrix element of $M(\hat{Q}, \hat{P})$, we define the displacement operator $D(\alpha, \alpha^*)$ by

$$\begin{aligned} D(\alpha, \alpha^*) &\equiv \exp(\alpha a^\dagger - \alpha^* a) \\ &= \exp(\text{Re}[\alpha](a^\dagger - a) + i \text{Im}[\alpha](a^\dagger + a)). \end{aligned} \quad (15)$$

Since the operator $M(\hat{Q}, \hat{P})$ can be written as

$$\begin{aligned} M(\hat{Q}, \hat{P}) &\equiv \exp\left[i\left(\hat{Q}\cos(\omega_d t/n) + \hat{P}\sin(\omega_d t/n)\right)\right] \\ &= \exp\left[-\sqrt{\frac{\lambda}{2}}\sin(\omega_d t/n)(a^\dagger - a) \right. \\ &\quad \left. + i\sqrt{\frac{\lambda}{2}}\cos(\omega_d t/n)(a^\dagger + a)\right], \end{aligned} \quad (16)$$

we get the relationship between the parameter α of $D(\alpha, \alpha^*)$ and parameters of $M(\hat{Q}, \hat{P})$

$$\begin{aligned} \alpha &\equiv -\sqrt{\frac{\lambda}{2}}\sin(\omega_d t/n) + i\sqrt{\frac{\lambda}{2}}\cos(\omega_d t/n) \\ &= \sqrt{\frac{\lambda}{2}}e^{i(\varphi+\pi/2)}, \end{aligned} \quad (17)$$

with $\varphi = \omega_d t/n$. We further define the following notations

$$\begin{aligned} \text{Coherent state : } |\alpha\rangle &\equiv e^{-\frac{1}{2}|\alpha|^2} \sum_{k=0}^{\infty} \frac{\alpha^k}{\sqrt{k!}} |k\rangle, \\ \langle\beta|\alpha\rangle &= e^{\alpha\beta^* - (|\alpha|^2 + |\beta|^2)/2}, \end{aligned}$$

$$\begin{aligned} \text{Displaced Fock state : } |\alpha, k\rangle &\equiv D(\alpha, \alpha^*)|k\rangle, \\ |0, k\rangle &= |k\rangle. \end{aligned} \quad (18)$$

According to Eq.(3.11) in the Ref. of *Quantum Opt.* 3, 359 (1991)²⁹, we have

$$\langle\beta, l|\alpha, k\rangle = \langle\beta|\alpha\rangle \sqrt{\frac{l!}{k!}} (\beta^* - \alpha^*)^{k-l} L_l^{k-l} \left\{ \frac{|\beta - \alpha|^2}{k} \right\}. \quad (19)$$

Here, $L_l^{k-l}(\bullet)$ is the Laguerre polynomials. Let $\beta = 0$, we have the exact form of matrix element of displacement operator $D(\alpha, \alpha^*)$

$$\begin{aligned} \langle l|\alpha, k\rangle &\equiv \langle l|D(\alpha, \alpha^*)|k\rangle \\ &= e^{-|\alpha|^2/2 + i\pi(k-l)} (\alpha^*)^{k-l} \sqrt{\frac{l!}{k!}} L_l^{k-l} (|\alpha|^2). \end{aligned} \quad (20)$$

Using the relationship (17) we get the explicit form of matrix elements of $M(\hat{Q}, \hat{P})$

$$\langle l|M(\hat{Q}, \hat{P})|k\rangle = e^{-\lambda/4+i(k-l)(\pi/2-\omega_d t/\hbar)} \sqrt{\frac{l!}{k!}} \left(\frac{\lambda}{2}\right)^{\frac{k-l}{2}} L_l^{k-l}(\lambda/2). \quad (21)$$

Thus, quantum Hamiltonian (14) is

$$\begin{aligned} H_{RF} &= \frac{1}{2\lambda} \hbar\delta\omega(\hat{Q}^2 + \hat{P}^2) + [Ae^{i\omega_d t} M(\hat{Q}, \hat{P}) + h.c.] \\ &= \hbar\delta\omega(a^\dagger a + \frac{1}{2}) + [Ae^{i\omega_d t} M(\hat{Q}, \hat{P}) + h.c.] \\ &= \hbar\delta\omega(a^\dagger a + \frac{1}{2}) + A \left[\sum_{k,l} \langle l|M(\hat{Q}, \hat{P})|k\rangle e^{i\omega_d t} |l\rangle\langle k| + h.c. \right] \\ &= \hbar\delta\omega(a^\dagger a + \frac{1}{2}) + A \left[\sum_{k,l} e^{i\omega_d t} e^{-\lambda/4+i(k-l)(\pi/2-\omega_d t/\hbar)} \right. \\ &\quad \left. \times \sqrt{\frac{l!}{k!}} \left(\frac{\lambda}{2}\right)^{\frac{k-l}{2}} L_l^{k-l}(\lambda/2) |l\rangle\langle k| + h.c. \right]. \quad (22) \end{aligned}$$

Under RWA, we drop the fast oscillating terms ($k-l \neq n$) and get RWA Hamiltonian ($k-l = n$)

$$\begin{aligned} H_{RWA} &= \hbar\delta\omega(a^\dagger a + \frac{1}{2}) + A \left[\sum_l e^{-\lambda/4+i n \pi/2} \right. \\ &\quad \left. \times \sqrt{\frac{l!}{(l+n)!}} \left(\frac{\lambda}{2}\right)^{\frac{n}{2}} L_l^n(\lambda/2) |l\rangle\langle l+n| + h.c. \right] \\ &= \hbar\delta\omega(a^\dagger a + \frac{1}{2}) + A \left[e^{-\lambda/4+i n \pi/2} \left(\frac{\lambda}{2}\right)^{\frac{n}{2}} \right. \\ &\quad \left. \times \sum_l |l\rangle\langle l+n| \sqrt{\frac{l!}{(l+n)!}} L_l^n(\lambda/2) + h.c. \right] \\ &= \hbar\delta\omega(a^\dagger a + \frac{1}{2}) + A \left[e^{-\lambda/4-i n \pi/2} \left(\frac{\lambda}{2}\right)^{-\frac{n}{2}} \right. \\ &\quad \left. \times \sum_l |l\rangle\langle l+n| \sqrt{\frac{(l+n)!}{l!}} L_{l+n}^{-n}(\lambda/2) + h.c. \right] \\ &= \hbar\delta\omega(a^\dagger a + \frac{1}{2}) + A \left[e^{-\lambda/4-i n \pi/2} \left(\frac{\lambda}{2}\right)^{-\frac{n}{2}} \right. \\ &\quad \left. \times \sum_l |l\rangle\langle l+n| L_{a^\dagger a}^{-n}(\lambda/2) + h.c. \right] \\ &= \hbar\delta\omega(a^\dagger a + \frac{1}{2}) + A \left[e^{-\lambda/4-i n \pi/2} \left(\frac{\lambda}{2}\right)^{-\frac{n}{2}} a^n L_{a^\dagger a}^{-n}(\lambda/2) + h.c. \right]. \quad (23) \end{aligned}$$

Here we have used the relationship²⁹ $L_l^n(x)/L_{l+n}^{-n}(x) = (-x)^{-n}(l+n)!/l!$ for $x > 0$. We now scale the RWA Hamiltonian by $\hbar\omega/\lambda$ and get the dimensionless Hamiltonian \hat{g}

$$\begin{aligned} \hat{g} &\equiv \frac{\lambda}{\hbar\omega} H_{RWA} \\ &= \lambda\epsilon(a^\dagger a + \frac{1}{2}) + \mu \left[e^{-\lambda/4-i n \pi/2} \left(\frac{\lambda}{2}\right)^{-\frac{n}{2}} a^n L_{a^\dagger a}^{-n}(\lambda/2) + h.c. \right], \quad (24) \end{aligned}$$

where the parameters $\epsilon = \delta\omega/\omega$ and $\mu = \lambda A/(\hbar\omega)$ are the dimensionless detuning and driving strength respectively.

Using the following asymptotic form of Laguerre polynomials^{30,31}

$$\lim_{k \rightarrow \infty} L_k^\alpha(x/k) = k^\alpha e^{\frac{x}{2k}} x^{-\alpha/2} J_\alpha(2\sqrt{x}), \quad (25)$$

we have the following relationship in the limit of $k, l \gg |k-l|$ for a fixed $k-l$

$$\begin{aligned} L_k^{k-l}(\lambda/2) &\approx e^{\lambda/4} k^{k-l} (k\lambda/2)^{-(k-l)/2} J_{k-l}(2\sqrt{k\lambda/2}) \\ &= e^{\lambda/4} \left(\frac{\lambda}{2k}\right)^{-\frac{1}{2}(k-l)} J_{k-l}(\sqrt{2k\lambda}). \quad (26) \end{aligned}$$

Thus, in the semiclassical limit, i.e., $k, l \rightarrow \infty$ and fixed $k-l$, Eq.(21) goes to the following

$$\begin{aligned} \langle l|M(\hat{Q}, \hat{P})|k\rangle &= e^{-\lambda/4+i(k-l)(\pi/2-\varphi)} \sqrt{\frac{l!}{k!}} \left(\frac{\lambda}{2}\right)^{\frac{k-l}{2}} L_l^{k-l}(\lambda/2) \\ &\approx e^{i(k-l)(\pi/2-\varphi)} k^{(k-l)/2} \sqrt{\frac{l!}{k!}} J_{k-l}(\sqrt{2k\lambda}) \\ &\approx e^{i(k-l)(\pi/2-\varphi)} J_{k-l}(\sqrt{2k\lambda}). \quad (27) \end{aligned}$$

Here, we have used the limit relationship $\sqrt{\frac{l!}{k!}} k^{(k-l)/2} \rightarrow 1$. Therefore, we have the RWA Hamiltonian (24) in the Fock representation $\hat{g} = \sum_{k=0, l=0}^{\infty} f(k, l) |k\rangle\langle l|$ with

$$f(k, l) \approx \lambda\epsilon(k + \frac{1}{2})\delta_{k,l} + \mu \left[e^{i n \frac{\pi}{2}} J_{k-l}(\sqrt{\lambda(k+l+1)}) \delta_{l-k, n} + h.c. \right]. \quad (28)$$

We define the radial and angular operators \hat{r} and $\hat{\theta}$ by $a = e^{-i\theta}\hat{r}/\sqrt{2\lambda}$ and $a^\dagger = \hat{r}e^{i\theta}/\sqrt{2\lambda}$. In the Fock representation, the operator $e^{i\hat{\theta}}$ is defined by

$$e^{i\hat{\theta}} = \sum_{k=0}^{\infty} |k\rangle\langle k+1|, \quad \text{and} \quad e^{-i\hat{\theta}} = \sum_{k=0}^{\infty} |k+1\rangle\langle k|. \quad (29)$$

Using the above relationships, we have the following Hamiltonian in the semiclassical limit $\lambda \rightarrow 0$

$$\hat{g} \rightarrow g = \frac{1}{2}\epsilon r^2 + 2\mu J_n(r) \cos(n\theta - \frac{n\pi}{2}). \quad (30)$$

B. Quantum tunnelling in phase space

In this section, we give a detailed description about the quantum tunnelling process in phase space and the analytical behavior of ‘‘momentum’’ θ in the complex plane. We also calculate the asymmetry factor δ and show its linear relationship with $1/\lambda$ for different bands. To be convenient, we define a new variable $\hat{\xi} \equiv \hat{r}^2/2$ here. The semiclassical Hamiltonian (30) can be rewritten as $g = \epsilon\xi + 2\mu J_n(\sqrt{2\xi}) \cos(n\theta - \frac{n\pi}{2})$ in new variables ξ and θ , which define the ‘‘ $\xi - \theta$ ’’ phase space for our WKB calculation. For a fixed g , the general solutions of classical orbits are

$$\theta_{\pm}(\xi, g) = \frac{\pi}{2} \pm \frac{1}{n} \arccos \left[\frac{g - \epsilon\xi}{2\mu J_n(\sqrt{2\xi})} \right] + k \frac{2\pi}{n}, \quad (31)$$

where $k = 0, 1, 2, \dots$, and $n - 1$ represent the n branches of solutions. Here, we choose the parameters $\epsilon = 0$ and $\mu = -1$. In Fig. 5, we show three classical orbits for a fixed $g < 0$. The two classical orbits in the first loop are indicated by red closed curves, which correspond to the following solutions

$$\begin{aligned}\theta_{\pm}(\xi, g) &= -\frac{\pi}{n} \pm \frac{1}{n} \arccos\left[\frac{g - \epsilon\xi}{2\mu J_n(\sqrt{2\xi})}\right], \quad \text{and} \\ \theta_{\pm}(\xi, g) &= \frac{\pi}{n} \pm \frac{1}{n} \arccos\left[\frac{g - \epsilon\xi}{2\mu J_n(\sqrt{2\xi})}\right].\end{aligned}\quad (32)$$

The classical orbit in the second loop is indicated by yellow closed curve, which corresponds to the following solution

$$\theta_{\pm}(\xi, g) = \pm \frac{1}{n} \left(\pi - \arccos\left[\frac{g - \epsilon\xi}{2\mu J_n(\sqrt{2\xi})}\right] \right). \quad (33)$$

In the regime of $|(g - \epsilon\xi)/[2\mu J_n(\sqrt{2\xi})]| < 1$, two real solutions $\theta_{\pm}(\xi, g)$ together represent one closed classical orbit $\theta(\xi, g)$. In Fig. 5(left), the boundaries of classical motions are indicated by the white dashed lines, i.e., ξ_1 , ξ_2 and ξ_3 . Beyond the classical boundaries, the value of $\theta(\xi, g)$ has imaginary part. In Fig. 5(right), we show the analytical structures of solutions $\theta_{\pm}(\xi, g)$ in the complex plane. The closed curves on the real axis of θ represent classical orbits (we deviate the orbits slightly from the real axis to illustrate the shapes of orbits). There are n identical orbital branches with only a $2\pi/n$ -shift of $\text{Re}[\theta]$ for each type of solution.

In the quantum regime, the classical orbits can tunnel into each other through the classical forbidden region. In Fig. 5(left), we show the quantum tunnelling process of the two states in the first loop in phase space. The corresponding behavior of $\text{Im}[\theta]$ is depicted in Fig. 5(right). Starting from the classical boundary ξ_2 to the zero point of Bessel function $\xi^{(0)}$, the imaginary part $\text{Im}[\theta]$ increases from zero to infinite, where it jumps to another branch of solution. Then it goes back from infinite to zero as ξ changes from $\xi^{(0)}$ to another classical boundary ξ_3 . After that, $\text{Im}[\theta]$ increases again from zero to infinite as ξ goes from ξ_2 to $\xi^{(0)}$, where it jumps again to another branch of solution. Finally, $\text{Im}[\theta]$ decreases from infinite to zero as ξ changes from $\xi^{(0)}$ to the classical boundary ξ_3 . As we have discussed in the main text, the amplitude of quantum tunnelling rate J_l is given by the integral of the imaginary part of ‘‘momentum’’ θ in the classical forbidden region $\xi_2 < \xi < \xi_3$

$$|J_l| = \frac{\lambda}{2\pi} \left(\frac{dS}{dg} \right)^{-1} \Big|_{g=g_l} \exp\left(-\frac{2}{\lambda} \int_{\xi_2}^{\xi_3} \text{Im}[\theta] d\xi\right). \quad (34)$$

The tunnelling process can also happen through lower boundary ξ_1 as indicated by the white arrows in Fig. 5(left). However, the lower path is much longer than the upper path. Thus, the contribution to $|J_l|$ from the lower path is exponentially smaller than the contribution from upper path.

The jumping processes between different branches of solutions give additional phases to the quantum tunnelling rate J_l , which makes it a complex number $J_l = |J_l|e^{-i\delta_l}$. As we have discussed in the main text, the connecting condition by jumping is given by the phase translation operator

$\hat{T}_{\tau} = e^{-i\tau\hat{a}^{\dagger}\hat{a}}$. Since $\xi^{(0)} \gg 1$, we can expand operator \hat{T}_{τ} by $\hat{a}^{\dagger}\hat{a} \approx \xi^{(0)}/\lambda + i\partial/\partial\theta$. As a result, the connecting condition is $\hat{T}_{\tau}\phi_l(\theta) \approx e^{-i\xi^{(0)}\tau/\lambda}\phi_l(\theta + \tau)$. Thus we get the symmetry factor

$$\delta_l = \delta_l^0 + \xi^{(0)}/\lambda, \quad (35)$$

where δ_l^0 is the residual asymmetry beyond WKB calculation. In Fig. 6(a), we compare the above linear relationships between δ_l and $1/\lambda$ for different bands to our numerical simulations. In Fig. 6(b) and Fig. 6(c), we expand the asymmetry factor to the whole field of real number \mathbb{R} and plot it as function of $1/\lambda$ for different bands. The bands in Fig. 6(b) are all in the first loop. We see that, since the states in the first loop tunnel through the upper boundary, they all have the same slope given by $\xi^{(0)}$, which is the second zero point of Bessel function $J_n(\sqrt{2\xi})$. Here, we consider $\xi^{(0)} = 0$ is the first zero point of Bessel function $J_n(\sqrt{2\xi})$ for $n \neq 0$.

In Fig. 6(c), we show the linear relationships between δ_l and $1/\lambda$ for the bottom bands in different loops. We see their slopes are different. The reason is that the bands in different loops tunnel through different paths with different jumping points $\xi^{(0)}$. Like the states in the first loop, the states in other loops can tunnel through both the upper boundary and lower boundary. However, we have checked the integral $\int \text{Im}[\theta] d\xi$ of the upper path is always larger than that of the lower path. Therefore, the contribution to the tunnelling rate from the upper path is exponentially smaller than the contribution from the lower path. Therefore, the slope of all the bands in the l -th ($l > 1$) loop is given by the l -th zero point $\xi_l^{(0)}$ of Bessel function $J_n(\sqrt{2\xi})$. In the following table, we compare the slopes extracted from numerical simulation to our theoretical calculation.

Band Index	$\xi^{(0)}$ (Numerical)	$\xi^{(0)}$ (Theory)	Relative Errors
I-1	642.241	651.545	-0.014
II-1	629.514	651.545	-0.034
III-1	860.600	844.308	0.019
IV-1	1021.829	1032.972	-0.011
V-1	1186.088	1225.435	-0.032
VI-1	1427.519	1424.378	0.002
VII-1	1662.219	1631.067	0.019
VIII-1	1820.811	1846.185	-0.014
IX-1	2056.534	2070.142	-0.007

C. Squeezing parameters v and u

In this section, we calculate the squeezing factor u of localized states near the stable points of phase space lattice. First, we determine the all the extrema (r_e, θ_e) including stable points and unstable saddle points by the derivatives of quasienergy (30) along both angular direction and radial di-

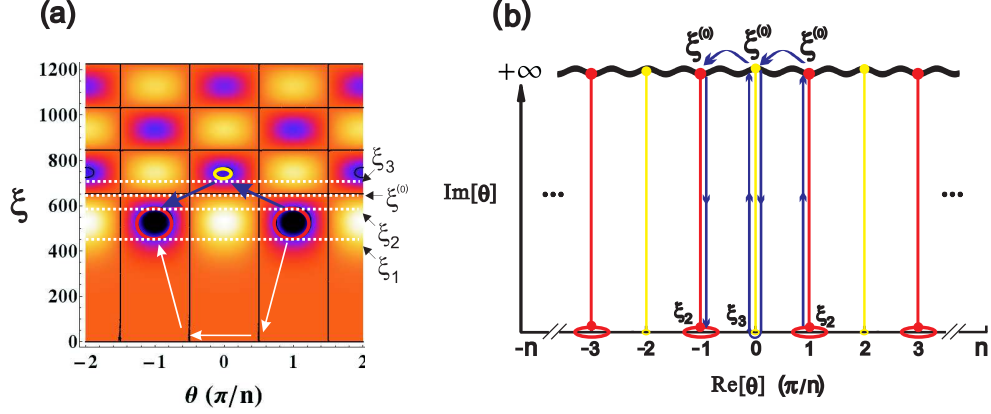


FIG. 5: **Quantum tunnelling in phase space.** a) Tunnelling processes of two states in the first loop. The red closed curves represent two classical orbits in the first loop. The yellow closed curve represents the classical orbit in the second loop. Parameters ξ_1 , ξ_2 and ξ_3 indicate the classical boundaries of classical motions. Parameter $\xi^{(0)}$ is the second zero point of Bessel function $J_n(\sqrt{2\xi})$. The blue arrows indicate the upper tunnelling path while the white arrows indicate the lower tunnelling path. b) Tunnelling diagram for calculating tunnelling rate J_l . We show the analytical behavior of θ in its complex plane. The red and yellow closed curves on the real axis $\text{Re}[\theta]$ correspond to the classical orbits with the same colors in the left figure (we deviate the orbits slightly from the real axis to illustrate the shapes of orbits). The red and yellow vertical lines correspond to the behaviors of imaginary parts $\text{Im}[\theta]$ in the classical forbidden region. The blue curves with arrows indicate the tunnelling process. The jumping processes happen at the zero point $\xi^{(0)}$ where the imaginary part $\text{Im}[\theta] = +\infty$.

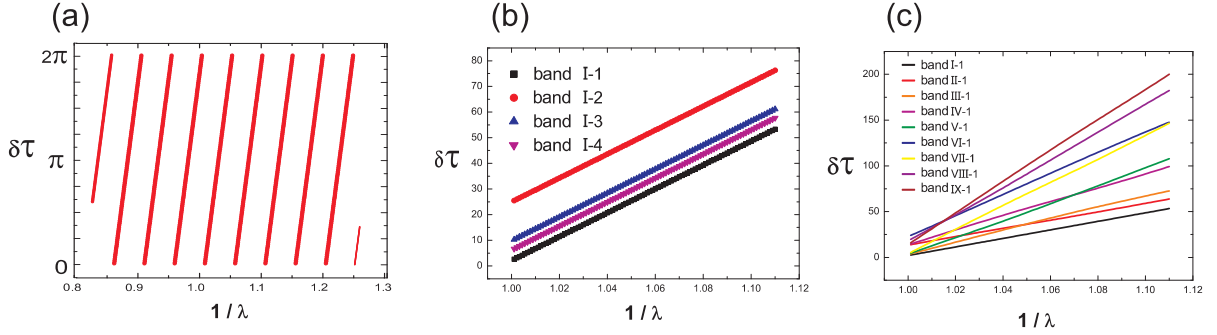


FIG. 6: **Asymmetry factors of bands.** a) Asymmetry factor (multiplied by $\tau = 2\pi/n$) of the first band (i.e., the bottom band in the first loop) as function of $1/\lambda$. b) Extended asymmetry factors (i.e., $\delta\tau \in \mathbb{R}$) of the first four bands in the first loop as function of $1/\lambda$. They all have the same slope. c) Extended asymmetry factors of the bottom bands in the first nine loops as function of $1/\lambda$. They have different slopes in general.

rection

$$\frac{\partial g}{\partial \theta} \Big|_{\theta=\theta_e, r=r_e} = -2n\mu J_n(r_e) \sin(n\theta_e - \frac{n\pi}{2}) = 0, \quad (36)$$

$$\begin{aligned} \frac{\partial g}{\partial r} \Big|_{\theta=\theta_e, r=r_e} &= \epsilon r_e + \mu (J_{n-1}(r_e) - J_{n+1}(r_e)) \\ &\quad \times \cos(n\theta_e - \frac{n\pi}{2}) = 0. \end{aligned} \quad (37)$$

The angular extrema can be obtained from Eq.(36), that is, $\theta_e = l\tau/2 + n\pi/2$ with $l = 0, \pm 1, \pm 2, \dots, \pm(n-1), n$, where $\tau = 2\pi/n$ is defined as *lattice constant* of phase space lattice. To get the radial extrema, we need to solve the equation (37). The stability of these extrema (r_e, θ_e) is determined by the second derivatives of g . If $(\partial^2 g / \partial \theta^2) \times (\partial^2 g / \partial r^2) \Big|_{r=r_e, \theta=\theta_e} > 0$, the extrema are stable, otherwise unstable. The second derivatives

to angle θ and radius r are

$$\frac{\partial^2 g}{\partial \theta^2} \Big|_{\theta=\theta_e, r=r_e} = -2n^2 \mu J_n(r_e) \cos(n\theta_e - \frac{n\pi}{2}), \quad (38)$$

$$\begin{aligned} \frac{\partial^2 g}{\partial r^2} \Big|_{r=r_e, \theta=\theta_e} &= \epsilon + \frac{1}{2} \mu (J_{n-2}(r_e) + J_{n+2}(r_e) - 2J_n(r_e)) \\ &\quad \times \cos(n\theta_e - \frac{n\pi}{2}). \end{aligned} \quad (39)$$

Below, we label the stable points (maxima and minima) and unstable saddle points by (r_m, θ_m) and (r_s, θ_s) respectively. We expand the quasienergy g near the stable points (r_m, θ_m) to the

second order

$$\begin{aligned}
g_{local} &\approx g(r_m, \theta_m) + \frac{1}{2} \frac{\partial^2 g}{r_m^2 \partial \theta^2} \Big|_{(r_m, \theta_m)} (r_m \theta - r_m \theta_m)^2 \\
&\quad + \frac{1}{2} \frac{\partial^2 g}{\partial r^2} \Big|_{(r_m, \theta_m)} (r - r_m)^2 \\
&= g(r_m, \theta_m) + \frac{\tilde{p}^2}{2m_e} + \frac{1}{2} m_e \omega_e^2 \tilde{x}^2.
\end{aligned} \tag{40}$$

Here, we have defined coordinate $\tilde{x} = r - r_m$ and momentum $\tilde{p} = r_m(\theta - \theta_m)$ near the stable point. The effective mass m_e and effective frequency ω_e are given by

$$m_e = r_m^2 \left(\frac{\partial^2 g}{\partial \theta^2} \right)^{-1} \Big|_{(r_m, \theta_m)} \quad \text{and} \quad \omega_e = \sqrt{m_e^{-1} \frac{\partial^2 g}{\partial r^2} \Big|_{(r_m, \theta_m)}}$$

respectively.

Now, we define the displacement operator $\hat{D}_\alpha = \exp(\alpha a^\dagger - \alpha^* a)$ and the squeezing operator $\hat{S}_\xi = \exp\left[\frac{1}{2}(\xi^* a^2 - \xi a^{\dagger 2})\right]$, which have the following properties

$$\hat{D}_\alpha^\dagger a \hat{D}_\alpha = a + \alpha, \quad \hat{S}_\xi^\dagger a \hat{S}_\xi = va + ua^\dagger$$

with $\xi = re^{i\theta}$. The squeezing parameters are given by $v = \cosh r$, $u = -e^{i\theta} \sinh r$. We transform the original \hat{g} to localized Hamiltonian \hat{g}_{local} at the stable point (r_m, θ_m) by three operators, i.e.,

$$\hat{g}_{local} = \hat{S}_\xi \hat{D}_\alpha \hat{T}_{\theta_m} \hat{g} \hat{T}_{\theta_m}^\dagger \hat{D}_\alpha^\dagger \hat{S}_\xi^\dagger.$$

Here, we first change the orientation using phase space rotation operator $\hat{T}_{\theta_m} = e^{-i\theta_m \hat{a}^\dagger \hat{a}}$. Then we move the Hamiltonian to the position of stable point using displacement operator $\hat{D}_\alpha = e^{\alpha a^\dagger - \alpha^* a}$. Finally, we squeeze the Hamiltonian to fit the stable point using squeezing operator $\hat{S}_\xi = e^{[\xi^* a^2 - \xi (a^\dagger)^2]/2}$. By choosing

$$\begin{aligned}
\alpha &= -\frac{r_m}{\sqrt{2\lambda}}, \quad v = \frac{1}{2} \left(\sqrt{m_e \omega_e} + \frac{1}{\sqrt{m_e \omega_e}} \right) \quad \text{and} \\
u &= \frac{1}{2} \left(\sqrt{m_e \omega_e} - \frac{1}{\sqrt{m_e \omega_e}} \right),
\end{aligned} \tag{41}$$

we get the localized Hamiltonian as following

$$\begin{aligned}
\hat{g}_{local} &= \hat{S}_\xi \hat{D}_\alpha \hat{T}_{\theta_m} \hat{g} \hat{T}_{\theta_m}^\dagger \hat{D}_\alpha^\dagger \hat{S}_\xi^\dagger \\
&= \lambda \omega_e (a^\dagger a + \frac{1}{2}) + g(r_m, \theta_m) + o(\lambda^2).
\end{aligned} \tag{42}$$

D. Effective temperature \bar{n}_e

We investigate the quantum dynamics near the bottom of a stable state. The dissipative dynamics is modified by squeezing and can be described by an effective temperature \bar{n}_e . The original master equation is

$$\frac{\partial \rho}{\partial \tau} = -\frac{i}{\lambda} [\hat{g}, \rho] + \kappa(1 + \bar{n}) \mathcal{D}[a] \rho + \kappa \bar{n} \mathcal{D}[a^\dagger] \rho. \tag{43}$$

The Lindblad superoperator is defined through $\mathcal{D}[A] \rho \equiv A \rho A^\dagger - (A^\dagger A \rho + \rho A^\dagger A)/2$, $\bar{n} = (e^{\hbar\omega_0/k_B T} - 1)^{-1}$ is the Bose distribution and κ is the dimensionless damping scaled ω . By performing a transformation on the density operator

$$\tilde{\rho} = \hat{S}_\xi \hat{D}_\alpha \hat{T}_{\theta_m} \rho \hat{T}_{\theta_m}^\dagger \hat{D}_\alpha^\dagger \hat{S}_\xi^\dagger,$$

we transform the master equation (43) into the following form³³

$$\begin{aligned}
\frac{d\tilde{\rho}}{d\tau} &= -i[\hat{g}_{local}, \tilde{\rho}] + \frac{\kappa}{2} \{(1 + \bar{n}_e) \mathcal{D}[a] \tilde{\rho} + \bar{n}_e \mathcal{D}[a^\dagger] \tilde{\rho}\} \\
&\quad + \frac{\kappa}{2} M (2a^\dagger \tilde{\rho} a^\dagger - a^{\dagger 2} \tilde{\rho} - \tilde{\rho} a^{\dagger 2}) + \frac{\kappa}{2} M^* (2a \tilde{\rho} a - a^2 \tilde{\rho} - \tilde{\rho} a^2).
\end{aligned} \tag{44}$$

Here, parameter $M = uv^*(2\bar{n} + 1)$ is the squeezing number. The effective Bose distribution is given by

$$\bar{n}_e = \bar{n}|v|^2 + (1 + \bar{n})|u|^2 = |u|^2 + \bar{n}(2|u|^2 + 1). \tag{45}$$

Near the bottom of stable points, we can make the harmonic approximation. The squeezing number $M = uv^*(2\bar{n} + 1)$ has no contribution to the stationary distribution. The ration of probability over adjoint levels thus is given approximately by³³ $\bar{n}_e/(1 + \bar{n}_e)$.

¹ L. Guo, M. Marthaler and G. Schön, *Phys. Rev. Lett.* **111**, 205303 (2013).

² E. Yablonovitch, *Phys. Rev. Lett.* **58**, 2059-2062 (1987); E. Yablonovitch, T. J. Gmitter and K. M. Leung, *Phys. Rev. Lett.* **67**, 2295-2298 (1991).

³ J. D. Joannopoulos, P. R. Villeneuve and S. Fan, *Nature* **386**, 143-149 (1997).

⁴ S. John, *Phys. Rev. Lett.* **58**, 2486-2489 (1987).

⁵ Z. V. Vardeny, A. Nahata and A. Agrawal, *Nature Photonics* **7**, 177-187 (2013).

⁶ E. L. Thomas, T. Gorishnyy and M. Maldovan, *Nature Materials* **5**, 773-774 (2006).

⁷ M. Choi *et al.* *Nature* **470**, 369-373 (2011).

⁸ J. T. Shen, P. B. Catrysse and S. Fan, *Phys. Rev. Lett.* **94**, 197401

(2005).

⁹ N. Fang *et al.* *Nature Materials* **5**, 452-456 (2006).

¹⁰ I. Bloch, *Nature Physics* **1**, 23-30 (2005).

¹¹ I. Bloch, J. Dalibard and W. Zwerger, *Rev. Mod. Phys.* **71**, 885-964 (2008).

¹² V. Gramich, B. Kubala, S. Rohrer and J. Ankerhold, *Phys. Rev. Lett.* **111**, 247002 (2013).

¹³ A.D. Armour, M.P. Blencowe, E. Brahimy and A.J. Rimberg, *Phys. Rev. Lett.* **111**, 247001 (2013)

¹⁴ M. Grifoni and P. Hänggi, *Phys. Rep.* **304**, 229 (1998).

¹⁵ M. O. Scully and M. S. Zubairy, *Quantum Optics*. Cambridge, 2009.

¹⁶ L. D. Landau and E. M. Lifshitz, *Quantum Mechanics (course of theoretical physics: v.3)*. Pergamon Press Ltd., 1977.

- ¹⁷ M. Marthaler and M. I. Dykman, *Phys. Rev. A* **76**, 010102 (R) (2007).
- ¹⁸ J. Struck *et al.* *Phys. Rev. Lett.* **108**, 225304
- ¹⁹ C. Rovelli, *Phys. Rev. Lett.* **83**, 1079 (1999)
- ²⁰ M. I. Dykman and V. N. Smelyanskiy, *Zh. Eksp. Teor.* **94**, 61 (1988) [*Sov. Phys. JETP* **67**, 1769 (1988)].
- ²¹ M. I. Dykman, *Phys. Rev. E* **75**, 011101 (2007).
- ²² L. Guo, *et al.* *Phys. Rev. E* **84**, 011144 (2011).
- ²³ S. Diehl, *et al.* *Phys. Rev. Lett.* **105**, 015702 (2010).
- ²⁴ M. I. Dykman, M. Marthaler and Peano, *Phys. Rev. A* **83**, 052115 (2011).
- ²⁵ W. K. Hensinger *et al.* *Nature* **412**, 52-55 (2001).
- ²⁶ Y. Makhlin, G. Schön and Shnirman, *Nature*, **398**, 305-307 (1999).
- ²⁷ A. N. Masluk *et al.* *Phys. Rev. Lett.*, **109**, 137002 (2012).
- ²⁸ C. Altimiras *et al.* *Appl. Phys. Lett.*, **103**, 212601 (2013).
- ²⁹ A. Wünsche, *Quantum Opt.* 3 (1991), 359-383.
- ³⁰ Harry Bateman, *Higher Transcendental Functions (Vol.2)*, Eq.(36) on page 191.
- ³¹ G. Szegő, *Orthogonal polynomials*, 4th edition, Amer. Math. Soc. Colloq. Publ., vol. 23, Amer. Math. Soc., Providence, RI, 1975, Eq.(8.22.1) on page 198.
- ³² C. Gerry & P. Knight, *Introductory Quantum Optics*, page 153, Cambridge (2005).
- ³³ Lingzhen Guo, *Quantum Effects in Driven Non-linear Systems*, Phd thesis on the website: <http://www.tfp.uni-karlsruhe.de/~lzguo/thesis.pdf>